



**POLITECNICO
MILANO 1863**

School of Industrial and Information Engineering
Department of Aerospace Science and Technology - DAER
MSc in Space Engineering

Final Project
Orbital Mechanics

**P.R.I.M.E. - Planetary Research and
Interplanetary Mission Explorer**

Group 2454

Professor: Camilla Colombo

Riccardo Coppola	279956	10773170
Nicolò Corbo	275318	10766366
Jonathan Jönsson	277226	11071847
Martina Spitalieri	270915	10764398

Delivery date: 07/01/2025
Academic Year 2024/2025

Contents

1 First Assignment: Interplanetary Explorer Mission	1
1.1 Introduction to the mission requirements	1
1.2 Multi-Step Grid Search	1
1.2.1 Preliminary considerations	1
1.2.2 Initial time windows and coarse grid search	2
1.2.3 Finer grid search	4
1.3 Full Windows Algorithms	5
1.3.1 Smart Search Algorithm	5
1.3.2 Particle Swarm Algorithm	6
1.4 Final result	7
1.4.1 Heliocentric trajectories	7
1.4.2 Flyby	7
1.4.3 Cost analysis	9
2 Second Assignment : Planetary Explorer Mission	9
2.1 Nominal orbit	10
2.2 Unperturbed ground track	10
2.3 Perturbed ground track	11
2.4 Propagation of the orbit	12
2.5 Real data analysis	13
References	14

1. First Assignment: Interplanetary Explorer Mission

1.1 Introduction to the mission requirements

The PoliMi Space Agency is conducting a feasibility study for a potential interplanetary explorer mission to visit an asteroid in the Solar System, with an intermediate flyby on a planet. Initial requirements are listed in Table 1.1.

Departing planet	Fly-by planet	Arrival asteroid	Earliest departure	Latest arrival
Earth	Jupiter	Asteroid N. 523649	00:00:00 01/01/2030	00:00:00 01/01/2060

Table 1.1: Mission requirements for Interplanetary Explorer mission

The figure of merit for this mission is the total cost, thus imposing a limit on the total budget: therefore, the minimization of transfer time will not be taken into account. Firstly, the design process will be presented, consisting of the study of the possible transfer options from the departure planet to the arrival one, taking into account the flyby at Jupiter, explaining the choice of time windows. The final solution will then be described in terms of Δv_{tot} . Both the heliocentric legs and the flyby will be analyzed through the patched conics method (note that planetary departure and insertion have not been considered, meaning the initial heliocentric orbit is equal to that of the Earth and the final orbit is equal to that of Asteroid 523649).

1.2 Multi-Step Grid Search

1.2.1 Preliminary considerations

Since the goal is to address a trajectory optimization problem over extended time windows, some preliminary considerations have been considered concerning the physical problem at hand.

Physical features of the three celestial bodies

The orbits of Earth and Jupiter are almost coplanar and circular, while Asteroid 523649 is on an elliptical orbit quite inclined with respect to the ecliptic plane. In order to study transfer opportunities, geometrical properties have been calculated and exploited to allow further reasoning. In particular, orbital periods for the three bodies and the coupled synodic periods are presented in Table 1.2.

Orbital periods	Synodic periods
$T_{\text{earth}} = 1 \text{ year}$	$T_{\text{syn}}^{\text{Earth-Jupiter}} = 1.0928 \text{ years}$
$T_{\text{jupiter}} = 11.8749 \text{ years}$	$T_{\text{syn}}^{\text{Jupiter-Asteroid}} = 27.0419 \text{ years}$
$T_{\text{asteroid}} = 21.1724 \text{ years}$	

Table 1.2: Orbital and synodic periods

As it can be seen, due to its different geometry the synodic period between Jupiter and the Asteroid covers almost the entire assigned time window; therefore, a different approach must be followed. As it will be later explained in Section 1.2.2, after one revolution of Jupiter, while it will face the asteroid plane in the same way, the asteroid itself will be located opposite to its starting configuration: this is because the orbital period of Jupiter is almost half the orbital period of the asteroid, meaning it will be influencing the cost of transfer between the two bodies.

Constraints applied

Some constraints have been considered in this analysis, such as:

- Minimum fly-by altitude at Jupiter: in order to avoid its atmosphere, a minimum altitude of 5000 km has been taken into account (this is reasonable since similar recent mission have reached also closer approaches, here a safety margin is considered [1])
- Maximum lifetime of the spacecraft to avoid transfers longer than the time span within which it is safe to consider all subsystems healthy and correctly functioning: here considered as 25 years
- Minimum time of flight must be higher than parabolic time of respective Lambert arc: $\text{TOF} > t_{\text{par}}$

Comparison with Hohmann transfers

In order to estimate a value of minimum Δv to validate the optimization results, two very simplified Hohmann transfers between the three bodies are computed, with all orbits coplanar, circular and with radii equal to their semi-major axes. This implies two strong assumptions: Asteroid 523649 is highly simplified and the maneuver at Jupiter is neglected. While the latter can be considered indeed negligible due to its very low cost, this is not true for the asteroid orbit, which is actually far from circular and not inclined. Therefore, these results will be used contextually.

$\Delta v_1 [\text{km/s}]$	$\Delta v_2 [\text{km/s}]$	$\Delta v_{\text{tot,Hohmann}} [\text{km/s}]$
9.8276	5.5906	15.4182

Table 1.3: Hohmann transfer cost

1.2.2 Initial time windows and coarse grid search

Analysis of modified porkchop plots

In order to analyze all possible transfers the combination of all possible dates of departure, gravity assist and arrival is necessary to find the optimal heliocentric legs solving the Lambert problem between the planets at their exact position given by their ephemerides. A strategy has been elaborated to restrict the time windows for a preliminary optimal transfer search. As shown in Figure 1.1, the two porkchop plots take into consideration the first insertion cost from Earth into the first Lambert arc and the last braking cost from the second Lambert arc to the asteroid, respectively, over the full assigned time windows. In addition, since the goal is to exploit these plots to identify repeating patterns in the low-cost zones that could aid the windows restrictions, for the second transfer Jupiter-Asteroid another plot is included spanning over 60 years, since it isn't possible to discern any particular frequency or pattern in 30 years only.

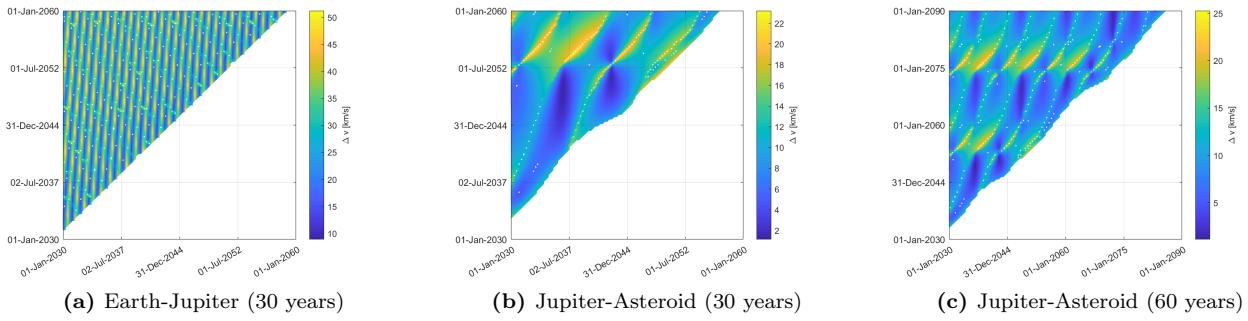


Figure 1.1: Modified porkchop plots

The cost pattern repetition shown is due to the periodicity of geometric configuration of the planets. For the Earth-Jupiter transfer, the frequency of low-cost zones is very regular and quite close to the synodic period between the two planets: this is due to Earth and Jupiter being almost coplanar on circular orbits (in fact, $e_{Earth} = 0.0167$, $e_{Jupiter} = 0.0485$, $i_{Earth} = 0$ deg, $i_{Jupiter} = 0.227$ deg). The same is not true for Jupiter and Asteroid 523649: due to their very different geometry, only two lost-cost zones can be identified in Figure 1.1b, with no repeating pattern between them. Only by enlarging the time window, it is possible to discern a clear repeating pattern: however, this is not related to the Jupiter-Asteroid synodic period, but to Jupiter's orbital period (more or less 12 years). With these considerations, since the low-cost stripes in the Earth-Jupiter plot intersect the low-cost zones in the Jupiter-Asteroid plot multiple times, it is reasonable to assume that the global minimum will lie in one of the two latter zones. Note that this reasoning still does not take into account the powered gravity assist, but the purpose of the first analysis will be to validate the concept that the possible global minimum lies on one of the two low-cost areas of the Jupiter-Asteroid porkchop plot.

Coarse grid search: time windows and results

The possible transfers will be analyzed by calculating Δv on each possible combination of time of departure, gravity assist and arrival, provided a certain discretization of the chosen preliminary time windows, and extracting the lowest cost of the grid. The latter will be the initial guess input to the MATLAB function *fmincon.m*, which will converge to the constrained minimum of the function with a gradient-based approach. Since *fmincon.m* is subject to convergence to local minima, and so it is highly dependent on the initial guess, finer and finer grids are needed to find the global minimum. The total cost of the mission, which is the merit parameter to minimize, involves three components of Δv :

- insertion from Earth's orbit to the first heliocentric leg towards Jupiter
- powered gravity assist at Jupiter
- insertion from the second heliocentric leg exiting from Jupiter to Asteroid 523649

The purpose of the first analysis will be to validate the concept that the possible global minimum lies on one of the two low-cost areas of the Jupiter-Asteroid porkchop plot, taking both into consideration since they are not the repetition of one another. The time windows are therefore defined as following and each analyzed with a timestep of 100 days:

- Gravity assist window will include both low-cost areas: **8/11/2032 12:00:00 - 13/4/2049 12:00:00**
- Departure window will begin at earliest possible date to the latest departure date in order to arrive at Jupiter at the latest fly-by date (constraints are always considered, meaning TOF is higher than t_{par}): **1/1/2030 00:00:00 - 30/11/2047 12:00:00**
- Arrival window will extend from the earliest arrival date if the fly-by is performed at the earliest possible date up to the maximum lifetime of the spacecraft from the earliest departure date: **13/11/2035 12:00:00 - 1/1/2055 00:00:00**

Leading to the following results:

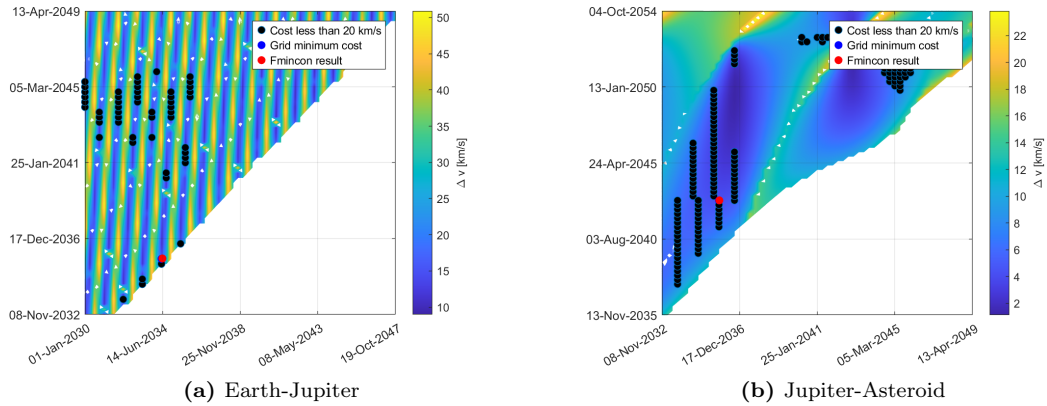


Figure 1.2: Coarse grid search: modified porkchop plots

As it can be noted from the plots, the grid minimum cost and the result of *fmincon.m* almost overlap, thus validating the hypothesis made above of the global minimum being in one of the two low-cost areas. Furthermore, the grid minimum cost is 16.1742 km/s while the *fmincon* result is 14.5269 km/s. A finer iteration is then needed to ascertain which of the two contains the global minimum.

1.2.3 Finer grid search

Two finer grid searches have been implemented restricting gravity assist windows on the two low-cost Jupiter-Asteroid transfer areas.

- First low-cost area:
 - Departure window: **1/1/2030 00:00:00 - 17/12/2036 12:00:00** with **30 days** timestep
 - Fly-by window: **8/11/2032 12:00:00 - 13/9/2039 12:00:00** with **30 days** timestep
 - Arrival window: **25/1/2041 12:00:00 - 1/1/2053 12:00:00** with **60 days** timestep
 - Second low-cost area:
 - Departure window: **17/12/2036 12:00:00 - 30/11/2047 12:00:00** with **30 days** timestep
 - Fly-by window: **25/1/2041 12:00:00 - 13/4/2049 12:00:00** with **60 days** timestep
 - Arrival window: **1/1/2047 00:00:00 - 1/1/2055 12:00:00** with **30 days** timestep

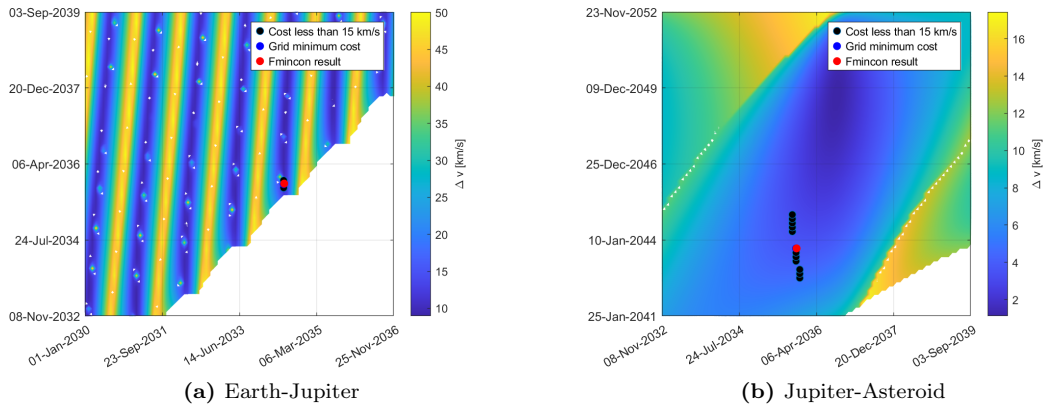


Figure 1.3: Finer grid search: earliest area

For the earliest low-cost area the optimization result is $\Delta v_{tot} = 14.4127$ km/s (instead of a grid minimum of $\Delta v_{tot} = 14.5501$ km/s), whereas for the second one is $\Delta v_{tot} = 18.4513$ km/s (instead of a grid minimum of $\Delta v_{tot} = 18.4873$ km/s).

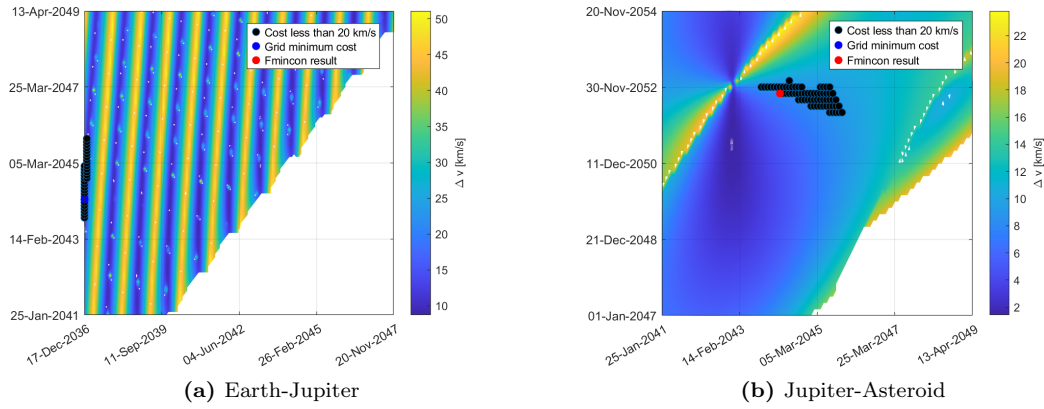


Figure 1.4: Finer grid search: latest area

1.3 Full Windows Algorithms

Another algorithmic approach for solving our problem aims to minimize the results in an almost fully automated manner over a long time interval, relying on minimal a priori considerations. This method was designed and implemented based on a single-step search, avoiding the need for lengthy, error-prone manual exploration relying on a problem that must necessarily be well-conditioned. This phenomenon also arises in our case, due to ambiguities caused by the large number of local minima and the extensive number of analyzable windows. To address this, we focused on making the code highly optimized while ensuring precision and robustness in identifying the correct minimum value.

This issue, related to the topology of our global cost function, is well illustrated by the following example graph of a function with numerous local minima, highlighting the multiple basins of attraction that could mislead global minimum search algorithms such as *fmincon*. Two methodological approaches have consequently been proposed to mitigate the occurrence of such phenomena:

- **Smart Search Algorithm:** A custom-designed algorithm based on a significant evolution and revision of the grid search, followed by a call to *fmincon*. The first part of the algorithm is modified to exhibit adaptive behavior and is highly optimized to discretize the entire search domain with sufficient precision.
- **Particle Swarm Algorithm:** A stochastic global optimization algorithm based on simulating the movement of a swarm of particles across the topology of our global cost function. Being stochastic doesn't guarantee convergence or repetitibility, and such we used multiple call of the algorithm.



Figure 1.5: Basins of Attraction [2]

It is of note that these methods were used in parallel to the Multi-Step Grid Search, in order to validate each other's results and confirm through different approaches the calculation of the global minimum, thus the best transfer possibility among the ones assigned.

1.3.1 Smart Search Algorithm

The core structure remains that of a grid search of the accumulation basin of the global minimum; however, it introduces significant computational advancements and optimizations. These do not directly aim to achieve faster computations but rather to reinvest the time saved to obtain a more accurate solution. The main differences compared to a classic grid search algorithm are as follows.

Constraints

The applied constraints are the same of the previous method, with the exclusion of the one on the maximum time for each Lambert arch, since the computation of the parabolic TOF actually is more computational consuming than the advantages it gives.

Removal of the Matrix Structure

The three nested loops, instead of assembling a three-dimensional tensor with high memory costs, retain only the value of the minimum and its position in temporal coordinates. During the iterations, the minimum value

is updated after calculating a smaller one. This approach allows for an increase in the number of sub-intervals without impacting the maximum performance provided by the memory.

Dynamic Windows

In each iteration, the temporal discretizations of the fly-by and arrival intervals are recalculated using a final time derived from the constraints and the current time, maintaining the originally desired resolution. This approach prevents the limited evaluation of maneuvers resulting from a very late departure, which would otherwise exclude earlier moments in time due to a static discretization.

Adaptive Δv Constraint

Adaptive exclusion of all iterations where the launch cost calculation already exceeds the total minimum stored so far. This approach dramatically reduces computational costs (as the first impulse is by far the most expensive) by skipping entire executions of the nested double loops. The method is also applied to the arrival cost calculation, though with less significant savings due to the lower magnitude of this maneuver's cost and its placement within nested calls. In practice, this results in the automation of the manual process of identifying all low Delta-V windows on the porkchop plot.

Specific Density Factors

Specific proportionality coefficients are used to determine the number of sub-intervals for the discretization intervals of each maneuver. This system enables optimal resource allocation for maneuvers that require higher precision. In our case, it is primarily applied to improve the discretization of the departure interval, which proportionally spans a much larger time frame compared to the subsequent mission intervals.

Blocks Scheme

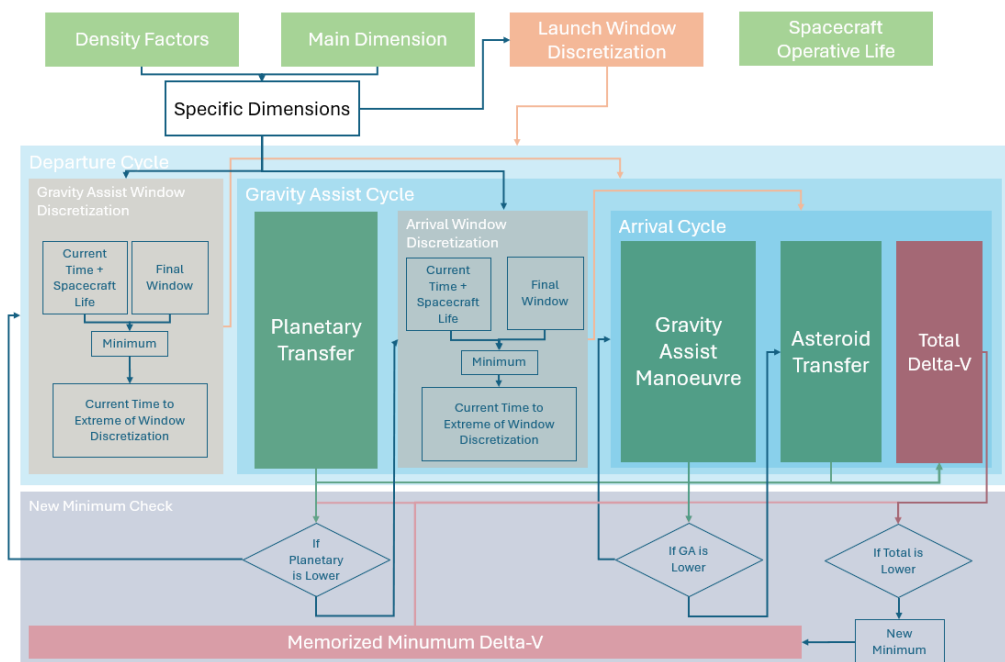


Figure 1.6: Smart Search Algorithm Diagram

Results

The algorithm demonstrates convergence to the identified minimum value of 14.4127 km/s, using at least the following call parameters:

$$\dim = 400, \quad \rho_{factors} = [3 \ 2 \ 2] \quad (1.1)$$

1.3.2 Particle Swarm Algorithm

A stochastic global optimization algorithm based on the emulation of a swarm of particles moving across the topology of the function. It does not rely on any a priori assumptions, and, due to its partially random formulation, it neither guarantees the reproducibility of results in a single application nor ensures absolute

convergence to the global minimum rather than a local minimum. Therefore, our approach involves multiple iterations of the method, recording the minimum value across all algorithm runs, which, with high probability, corresponds to the absolute minimum.

The algorithm, with 20 iterations, achieves convergence to the global minimum value already identified by other methods in a relatively short time, 880s.

1.4 Final result

1.4.1 Heliocentric trajectories

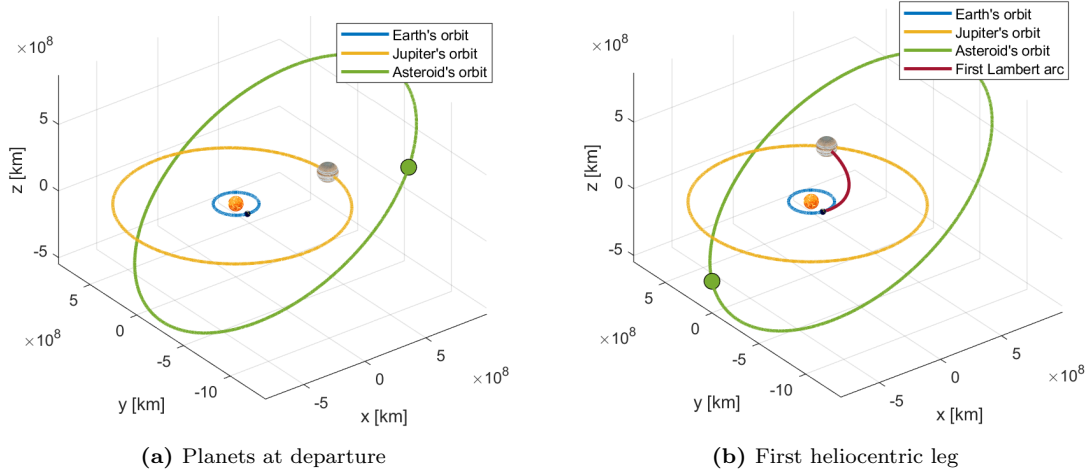


Figure 1.7: First interplanetary arc

In Figure 1.7 are presented the relative positions at departure on **13/06/2034 03:49:42** among the three celestial bodies, as well as the transfer arc (Earth and Asteroid are still depicted at departure, whereas Jupiter is plotted at fly-by date), which is characterized by the following Keplerian parameters:

Semi-major axis [km]	Eccentricity [-]	Inclination [deg]	RAAN [deg]
$7.3485 \cdot 10^8$	0.7933	1.7728	82.2480
Argument of pericenter [deg]	θ_{dep} [deg]	θ_{arr} [deg]	TOF [year]
179.3822	0.6178	143.0998	1.3775

Table 1.4: Keplerian elements of the first Lambert arc

As for the flyby, which occurs on **28/10/2035 22:41:30** with the configuration of planets as shown in Figure 1.8a, its characterization is possible through the final velocity at Jupiter on the first Lambert arc, which is $\mathbf{v}_{t,f}^{Earth-Jupiter} = [1.7890, 13.1317, -0.00004]$ km/s, and the initial velocity on the second Lambert arc (depicted in Figure 1.8b and whose parameters are listed in Table 1.5) which is $\mathbf{v}_{t,i}^{Jupiter-Asteroid} = [-13.4028, 3.1732, -6.2705]$ km/s.

Semi-major axis [km]	Eccentricity [-]	Inclination [deg]	RAAN [deg]
$1.0432 \cdot 10^9$	0.5363	28.7462	222.7745
Argument of pericenter [deg]	θ_{dep} [deg]	θ_{arr} [deg]	TOF [year]
272.5176	269.7276	158.1769	7.8792

Table 1.5: Keplerian elements of the second Lambert arc

Finally, the spacecraft reaches Asteroid 523649 on **12/09/2043 20:31:33**: the relative position of the three celestial bodies on this date is shown in Figure 1.9a. The combination of both heliocentric legs describing the total transfer from Earth to Asteroid 523649 with a fly-by at Jupiter is depicted in Figure 1.9b.

1.4.2 Flyby

The flyby hyperbola is completely characterized, since the incoming and outgoing heliocentric velocities are known. As mentioned in Section 1.2.1, a constraint was imposed on the fly-by, specifically that the minimum

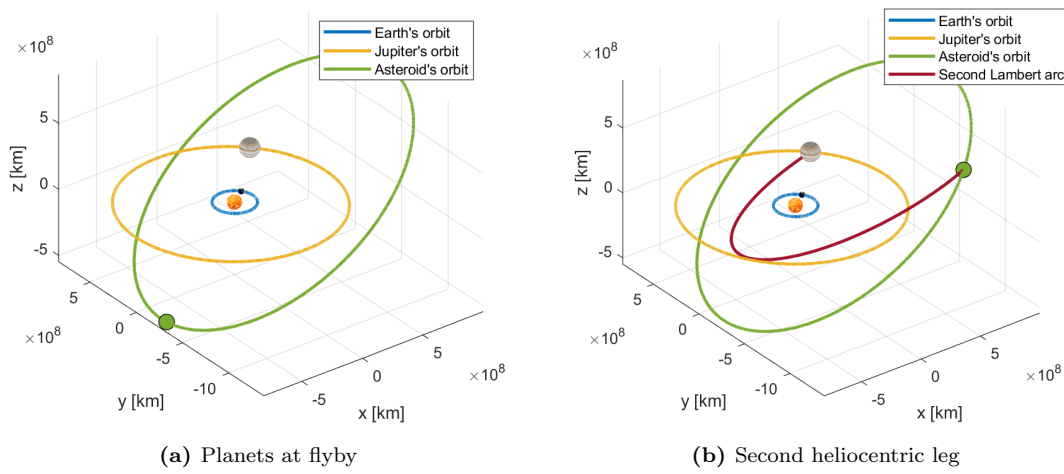


Figure 1.8: Second interplanetary arc

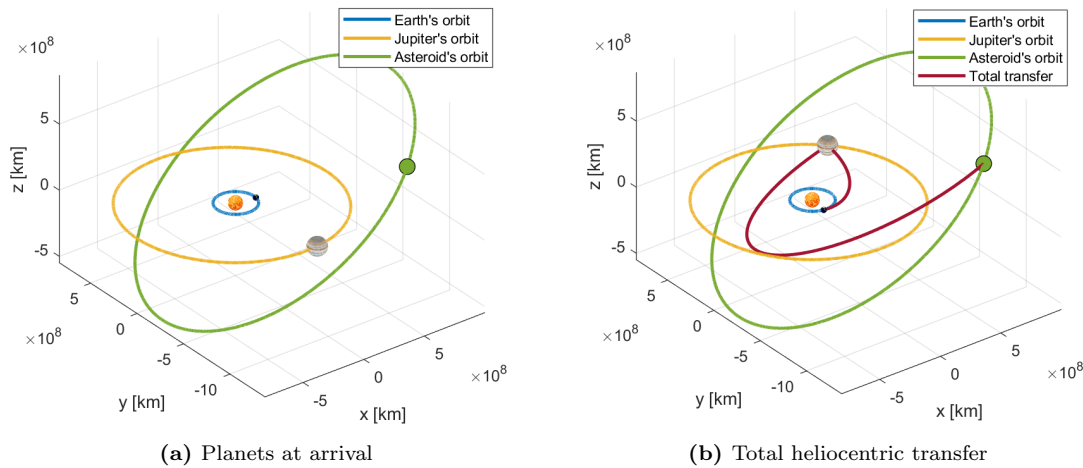


Figure 1.9: Second interplanetary arc

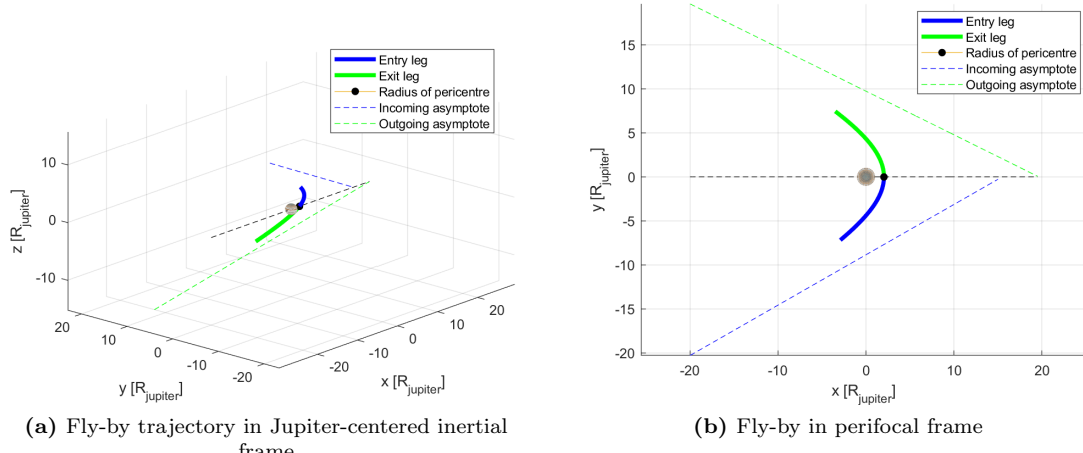


Figure 1.10: Fly-by trajectory

fly-by altitude must be equal to or above 5000 km, to avoid an aerobraking maneuver. Bearing this in mind, the results obtained from the calculations of the fly-by trajectory are listed in Table 1.6.

Δt_{SOI} represents the total time spent by the spacecraft inside the sphere of interest of Jupiter, which boundaries are computed with the equation ([3])

a^- [km]	a^+ [km]	e^- [-]	e^+ [-]	v_∞^- [km/s]	v_∞^+ [km/s]
$-9.3972 \cdot 10^5$	$-1.2301 \cdot 10^6$	1.1519	1.1160	[11.1523, 3.2310, -0.1667]	[-4.0395, -6.7275, -6.4371]
r_p [km]	h_{ga} [km]	δ [deg]	Δv_{flyby} [km/s]	$\Delta v_{powered}$ [km/s]	Δt_{SOI} [days]
$1.4271 \cdot 10^5$	$7.2802 \cdot 10^4$	123.8875	19.2166	0.3656	90.806

Table 1.6: Fly-by results

$$r_{SOI} = R_{Sun-Jupiter} \left(\frac{m_{Jupiter}}{m_{Sun}} \right)^{\frac{2}{5}} \quad (1.2)$$

The fly-by time of flight has been obtained through the hyperbolic time law: it corresponds to the 2.62% of the total time of flight, as seen in Table 1.8.

1.4.3 Cost analysis

The mission cost is summarized in Table 1.7.

First heliocentric leg [km/s]	Fly-by [km/s]	Second heliocentric leg [km/s]	Total cost [km/s]
10.3077	0.3656	3.7394	14.4127
71.52%	2.54%	25.95%	

Table 1.7: Summary of mission cost

As it is easily understood, the most expensive impulsive manoeuvre is the insertion of the spacecraft from Earth's orbit in the first heliocentric arc: in fact, the first Δv corresponds to more than 70% of the total cost. On the other hand, the fly-by proves quite efficient: the powered impulse the spacecraft required is very low whereas the free gravity-assist Δv the spacecraft receives from Jupiter is 19.217 km/s, very high and efficient since the orbital energy necessary to reach the Asteroid's orbit is higher. It is worth of notice how the preliminary estimation with Hohmann transfers presented in Section 1.2.1 proved itself wrong: this is because it is not possible to have two close-to-Hohmann transfer arcs since in the case of a flyby between two ideal Hohmann arcs, the heliocentric velocity must be parallel to the planet velocity both before and after the flyby, thus a turning angle of 180° is needed and a zero radius of pericenter would result. Having imposed a minimum altitude constraint, this explains why the previous estimation was helpful for an initial idea only. Nevertheless, it was useful to have a preliminary estimation of the magnitude of the total cost of the mission. Even though it was not considered as a figure of merit for this mission analysis, in Table 1.8 the TOF of each leg are summarized, each with its own percentage of the total time of flight.

First heliocentric leg [years]	Fly-by [days]	Second heliocentric leg [years]	Total time [years]
1.3775	90.806	7.8792	9.5055
14.49%	2.62%	82.89%	

Table 1.8: Summary of mission time

2. Second Assignment : Planetary Explorer Mission

The PoliMi Space Agency wants to launch a Planetary Explorer mission to perform Earth observation. The team was requested to conduct a planetary explorer mission around planet Earth, with given data to define the nominal orbit and the perturbations to which it is subject. Specifically, the investigation revolves around how J2 and atmospheric drag perturbations affect the Keplerian elements. This analysis will be performed following two different propagation techniques, the first using Gauss planetary equations and the second using Cartesian coordinates. Lastly, an analysis of two real objects' ephemerides is conducted, along with a comparison between the downloaded ephemerides and those calculated with the propagation model used for this study.

2.1 Nominal orbit

The nominal orbit of the Planetary Explorer Mission is described in Table 2.1, where values of Ω , ω and initial true anomaly were chosen arbitrarily.

a [km]	e [-]	i [deg]	Ω [deg]	ω [deg]	θ [deg]
12860	0.4893	52.47	15	15	15

Table 2.1: Keplerian parameters of nominal orbit

The orbit is prograde and has very high values of semi-major axis and eccentricity, typical of a HEO orbit, as depicted in Figure 2.1. Therefore, there is a noticeable difference in altitude at pericentre and apocentre as the minimum altitude is 196.6 km, while the maximum is 12781 km, meaning that the atmospheric drag will be present mainly close to the pericentre, while it will be negligible in other points. It is expectable that over long time period the atmospheric drag will reduce and circularize the orbit, leading to a decrease of semi-major axis and eccentricity, while the J2 effect will determine the secular variations of RAAN, argument of pericentre and mean anomaly. The nominal orbit has a period of 4 h 1 min 53 sec, which will be the reference time for further analysis.

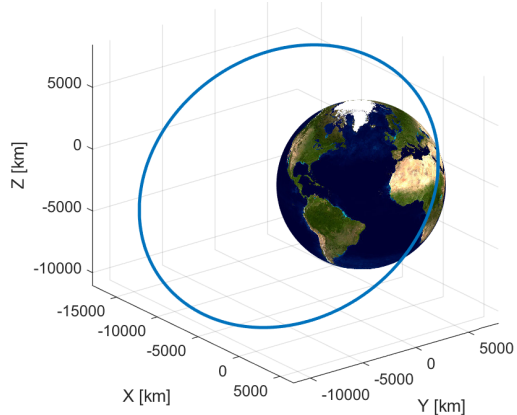


Figure 2.1: Nominal orbit

For the planetary explorer mission, the interest is analyzing the ground track of the orbit, both in the nominal case and in the repeating case, for which a different value of semi-major axis may be determined to achieve the desired repetition.

Ground track of nominal orbit

Nominal orbits' ground tracks were plotted over different relevant times, respectively one orbital period, ten orbital periods and ten days.

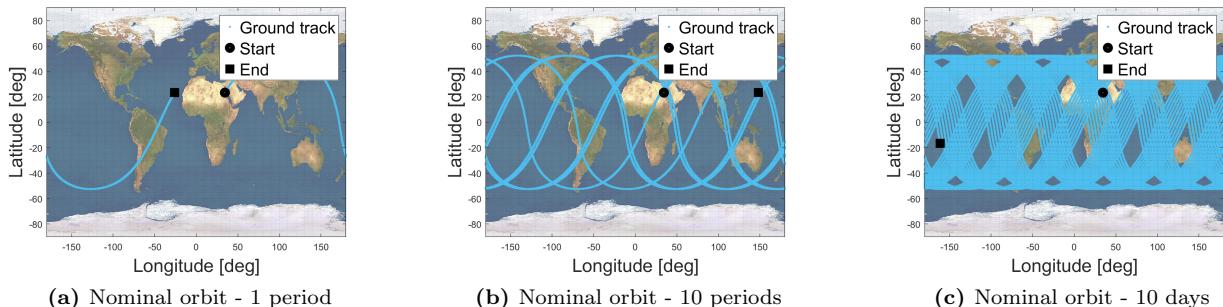


Figure 2.2: Nominal orbit over different time periods

Ground track of repeating orbit

The repeating orbit should guarantee $k = 14$ revolutions of the satellite for every $m = 3$ rotations of the planet, and it is defined with the same orbital parameters of the nominal orbit, a part from the semi-major axis that has to be modified to achieve repetition. It easily computed from the formula of mean motion

$$n = \frac{k}{m} \omega_{\oplus} = \frac{14}{3} \omega_{\oplus} \quad (2.1)$$

which leads to the definition of the semi-major axis to be 15099.4 km, with a corresponding orbital period $T_r = 5$ h 7 min 45 sec. The ground tracks of the repeating orbit were plotted for 14 orbital periods in Figure 2.3, in order to visualize the first repetition of the graph. The repeating ground track has initial and final points in the same position, unlike the nominal ground track.

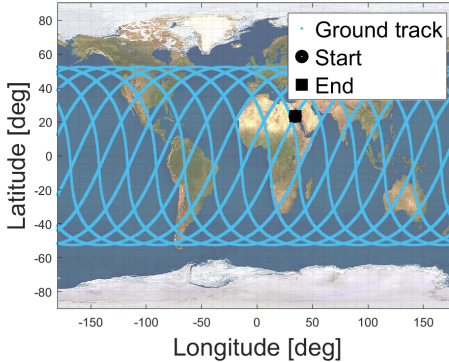


Figure 2.3: Repeating orbit - 14 periods

2.3 Perturbed ground track

In this analysis, Earth oblateness and atmospheric drag effects will be considered to affect the orbits and their ground tracks. For this application the perturbations are added as additional accelerations in the Cartesian formulation of the two-body-problem:

$$\frac{d^2\mathbf{r}}{dt^2} = \frac{-\mu_{\oplus}}{r^3}\mathbf{r} + \mathbf{a}_{J2} + \mathbf{a}_{Drag} \quad (2.2)$$

where the perturbing accelerations are computed at each time-step as:

$$\mathbf{a}_{J2}^{xyz} = \frac{3}{2} \frac{J_2 \mu_{\oplus} R_{\oplus}^2}{r^4} \begin{bmatrix} \frac{x}{r} \left(5 \frac{z^2}{r^2} - 1 \right) \\ \frac{y}{r} \left(5 \frac{z^2}{r^2} - 1 \right) \\ \frac{z}{r} \left(5 \frac{z^2}{r^2} - 1 \right) \end{bmatrix} \quad \text{and} \quad \mathbf{a}_{drag} = -\frac{1}{2} \frac{A_{cross} C_D}{m} \rho(h, t) v_{rel}^2 \frac{\mathbf{v}_{rel}}{\|\mathbf{v}_{rel}\|} \quad \text{where} \quad \mathbf{v}_{rel} = \frac{d\mathbf{r}}{dt} - \omega_{\oplus} \times \mathbf{r} \quad (2.3)$$

where the drag coefficient C_D was set at 2.1 and the surface to mass ratio $\frac{A}{m}$ is $0.0157 \frac{m^2}{kg}$.

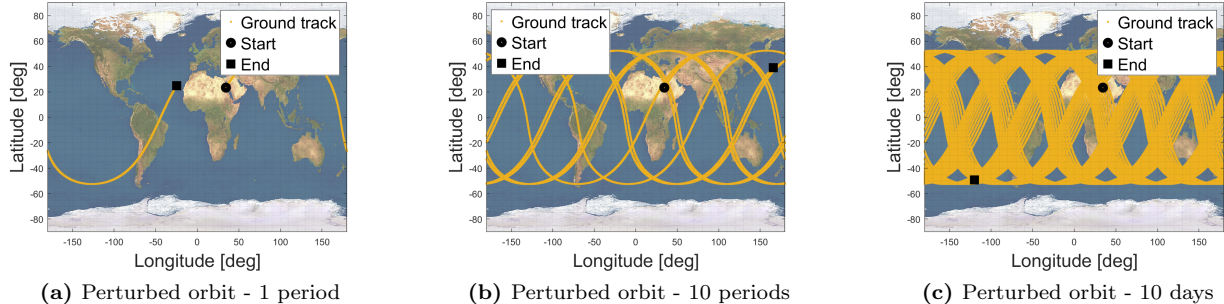


Figure 2.4: Perturbed orbit over different time periods

For the values of atmospheric density, it was considered an exponentially decreasing model with altitude:

$$\rho(h, t) = \rho_0 \exp \left(-\frac{h - h_0}{H} \right) \quad (2.4)$$

where the values of reference density ρ_0 , scale height H and reference altitude h_0 are tabulated for different altitudes as presented in [4]. Gauss planetary equations instead describe the effect of perturbations directly as variations of the Keplerian elements and they will be applied for the following tasks. Ground track of the perturbed orbit with modified semi-major axis to obtain repetition is depicted in Figure 2.5. The ground tracks of the perturbed orbits show non-negligible differences with respect to their equivalent plot for the ideal two-body problem. The only exception is

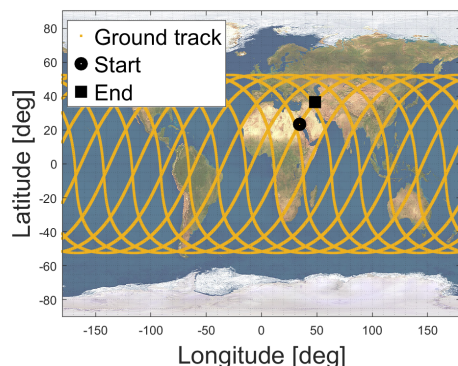


Figure 2.5: Perturbed repeating orbit - 14 periods

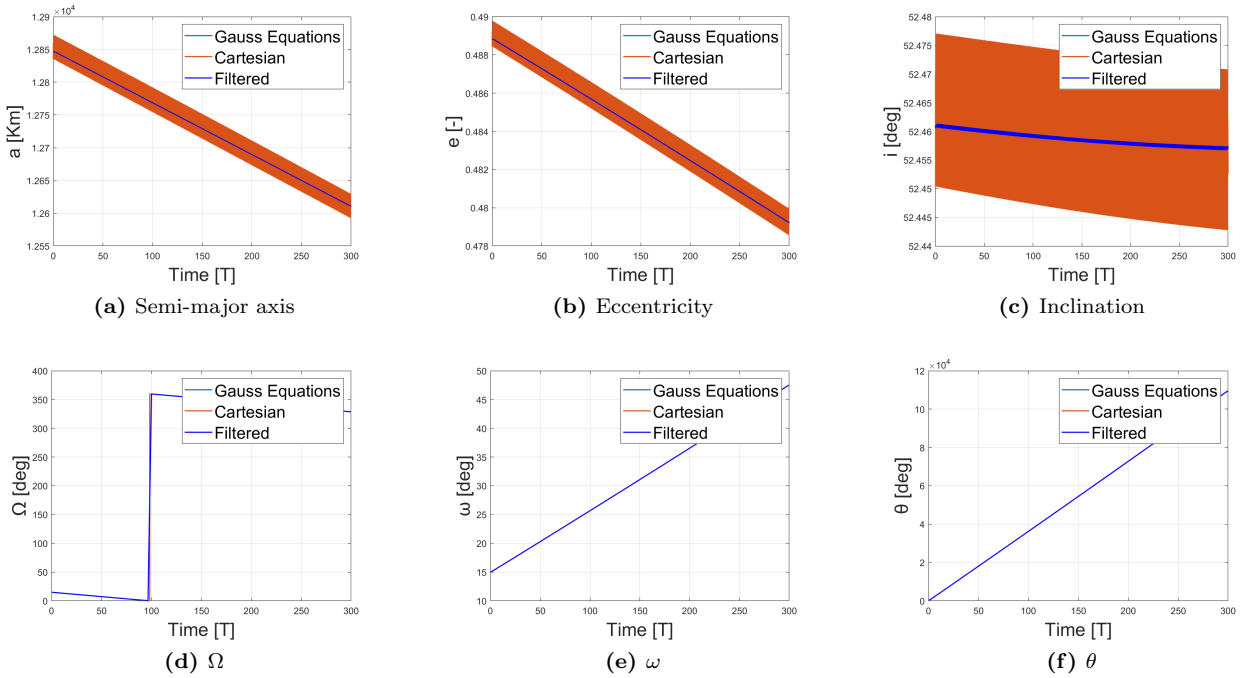
the ground track of the perturbed nominal orbit over one period, that is a time span too short to visually appreciate the effect of perturbations. Furthermore, the perturbed orbit with the modified semi-major axis does not repeat anymore like it did in the unperturbed case. The change of semi-major axis and of other parameters due to perturbations makes the orbit repetition after 3 revolutions of the Earth and 14 revolutions of the satellite impossible.

2.4 Propagation of the orbit

In order to propagate the initial orbit and hence determine the corresponding time evolution of the orbital elements, both the Cartesian formulation and the Gauss planetary equations were implemented and compared. Furthermore, for both methods, a limit situation was defined, specifically when the altitude at the pericentre is lower than 30 km, as the closer the S/C gets to the Earth's surface, the less precise the model will be. In the following simulations, such condition was never reached.

Evolution of keplerian elements in time

The evolution of Keplerian elements was performed over 300 periods of the initial orbit, corresponding to 50 days 9 h 27 min. Such time window has been considered sufficient to visualize the effect of circularization and size reduction of the air drag, as well as the J_2 effect short-term oscillations and secular changes on Ω , ω and mean anomaly. Furthermore, a filter was applied to extract the long-term evolutions of the parameters. The filter was coded with the *movemean* function of MATLAB, acting as a low-pass filter, where the period of the oscillations to discard T_{cut} was set to be equal to 7 initial orbital periods, or equivalently 1 day 4 h 13 min. Such filter properly follows the long-term variations of all the orbital parameters. Figures 2.7a and 2.7b show exactly the



effects of air drag mentioned previously, while secular variations are also visible in Figures 2.6d, 2.6e and 2.6f. The inclination of the orbit shows instead very little changes, as the J_2 effect and air drag have a low impact for the considered time window. It has also been experienced that there is no difference in terms of accuracy between the two methods considered. In fact, in all the figures the line representing the Cartesian propagation and Gaussian one are perfectly overlapped. This was verified by computing the maximum relative error for each parameter that occurred during the simulations, which were collected in Table 2.2. All the maximum relative errors were verified to be well below 10^{-5} , meaning that the curves show no difference at naked eye.

Orbit evolution in the considered time frame is depicted in Figure 2.6: the orbit has been propagated to observe how its shape and orientation would change throughout the considered time span, provided that no orbit-maintenance manoeuvre is performed. In both figures the change in right ascension of the ascending node and argument of pericentre is visible, together with the reduction of the semi-major axis and circularization of the orbit.

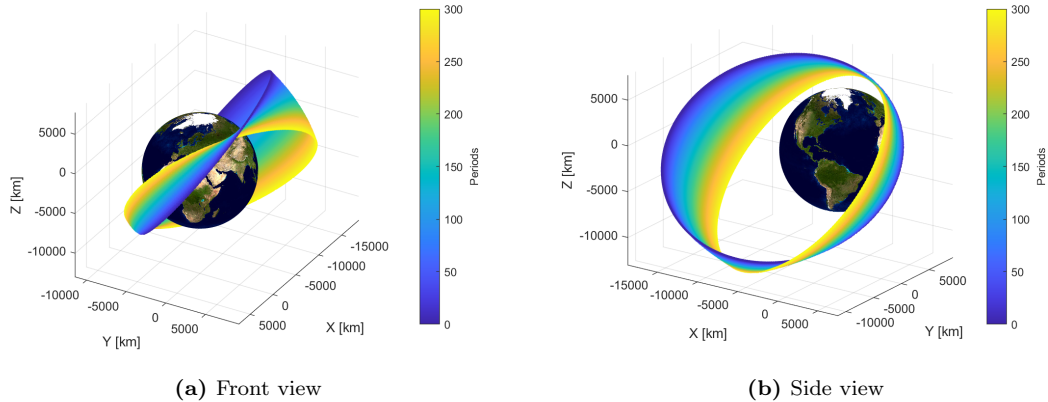


Figure 2.6: Front and side view of perturbed propagated orbit

$\frac{a_{cart} - a_{gauss}}{a_0}$ [km]	$\frac{e_{cart} - e_{gauss}}{e_0}$ [-]	$\frac{i_{cart} - i_{gauss}}{i_0}$ [deg]
$1 \cdot 10^{-8}$	$1.1 \cdot 10^{-8}$	$1.2 \cdot 10^{-9}$
$\frac{\Omega_{cart} - \Omega_{gauss}}{\Omega_0}$ [deg]	$\frac{\omega_{cart} - \omega_{gauss}}{\omega_0}$ [deg]	$\frac{\theta_{cart} - \theta_{gauss}}{\theta_0}$ [deg]
$7.8 \cdot 10^{-9}$	$2.4 \cdot 10^{-8}$	$8.7 \cdot 10^{-6}$

Table 2.2: Maximum relative errors on each Keplerian parameter

2.5 Real data analysis

As a final, an analysis of the evolution of the Keplerian parameters from NASA HORIZONS of two real objects was conducted, together with a comparison with the results produced by the model used previously. The first real body was chosen to be in the same orbital region as the nominal orbit of the previous tasks, therefore the selected object needs to have low altitude at pericentre and high altitude at apocentre, corresponding to a HEO orbit. Such research led to the choice of the FALCON 9 R/B rocket body (NORAD cat ID: 62260), with altitude at pericentre of around 210 km and at apocentre of 23500 km. The orbit was propagated for ten days from 16/12/2024 to 26/12/2024, leading to the results in Figure 2.7.

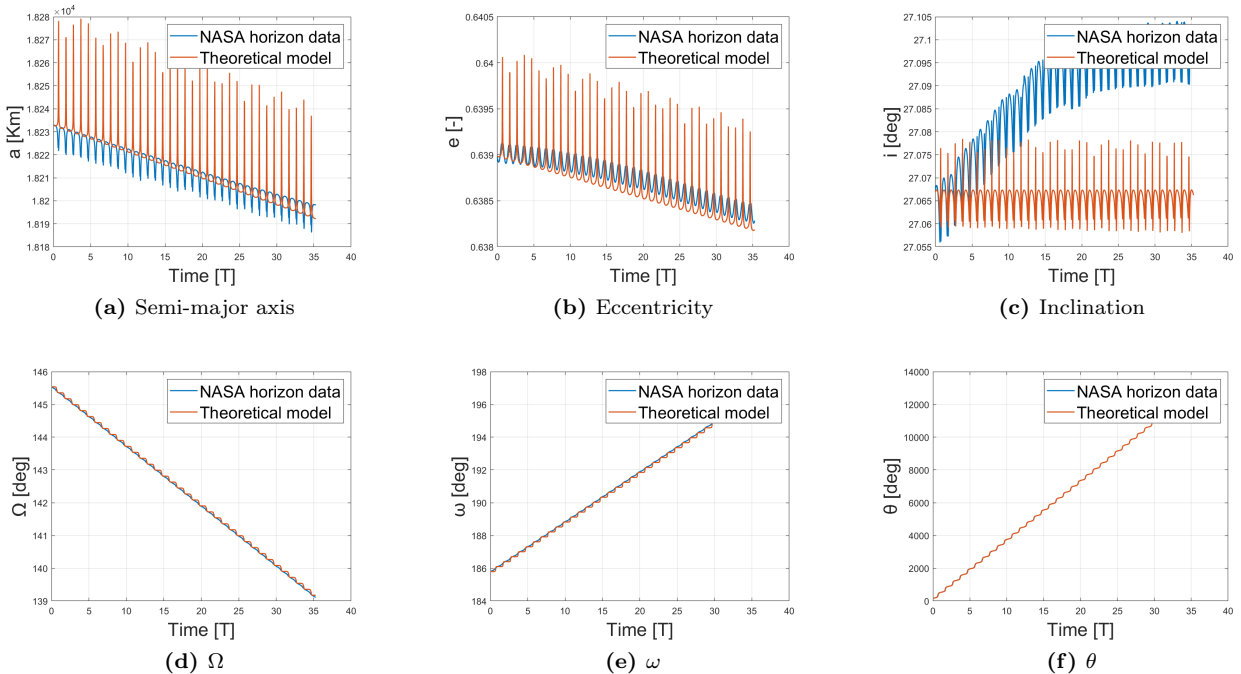


Figure 2.7: Falcon 9: Keplerian elements evolution

The second object was chosen to be a debris in LEO orbit (NORAD cat ID: 60781) which should be more exposed to the J_2 effect, for which the analysis was conducted in the same time span. The model follows

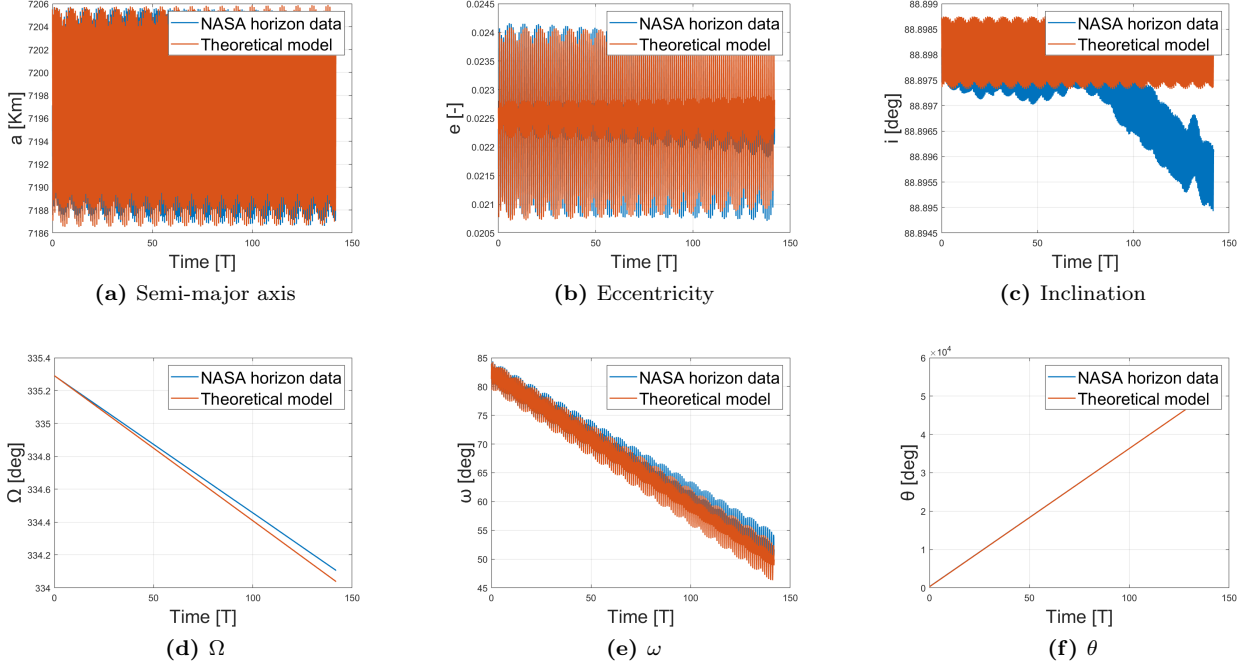


Figure 2.8: Debris: Keplerian elements evolution

properly the evolution of Ω , ω and true anomaly for both objects, while for the other parameters it has a better fitting for the debris, as such object is located in a LEO orbit, where the gravitational interference of the Moon, Sun and the solar radiation pressure are less important than the perturbations we considered. The oscillations of semi-major axis, eccentricity and inclination for the debris have a very short period and almost zero mean, which is a clear effect of the domination of the J_2 effect for this orbit, that leads also to the linear changes in Ω , ω and true anomaly.

On the other hand the rocket body flies on a very large and elliptical orbit, meaning that other perturbations like the gravity of the Moon, of the Sun or the solar radiation pressure may become important; since the model we applied does not consider them, this leads to more visible errors with respect to the NASA HORIZONS data. Nevertheless, the effect of air drag is clearly visible in the decay of the semi-major axis and eccentricity just like it was experimented in the previous tasks, as the low altitude at the pericenter makes this orbit very susceptible to such disturbance, while the J_2 effect affects again the short time oscillations in all the parameters and the linear variations of in Ω , ω and true anomaly.

References

- [1] INAF. *JUNO probe successfully completes first Jupiter flyby*. 2016. URL: <http://www.inaf.it/en/inaf-news/juno-probe-successfully-completes-first-jupiter-flyby>.
- [2] Mathworks. *Basins of Attraction*. URL: <https://it.mathworks.com/help/optim/ug/local-vs-global-optima.html>.
- [3] Howard D. Curtis. *Orbital mechanics for engineering students*. Butterworth-Heinemann, 2014.
- [4] Camilla Colombo. *Orbital Mechanics Course notes*. A.Y. 2024/2025.